

Quantum-limit phenomena and band structure in the magnetic topological semimetal EuZn_2As_2

Joanna Blawat ^{1,2}, Smita Speer², John Singleton³, Weiwei Xie⁴ & Rongying Jin ^{1,2}✉

The interplay between magnetism and electronic topology in the quantum limit is a forefront subject of condensed matter physics. Here, we show the electronic and magnetic properties of layered antiferromagnet EuZn_2As_2 in pulsed magnetic fields up to 60 T and temperatures down to 0.6 K. By analyzing the quantum oscillations observed in the magnetoresistance (MR) and proximity detector oscillator (PDO) frequency, we find that (1) the oscillation frequency $F = 46 \pm 6$ T for $H // c$ and 42 ± 2 T for $H // ab$; (2) the corresponding Berry phase is close to π for $H // c$, implying a nontrivial topology; and (3) the large linear MR occurs beyond the first Landau level, without any sign of saturation. From these observations, we conclude that the linear MR can be understood by considering diffusing cyclotron centers due to compressed Landau wavefunction, an emergent behavior in the quantum limit.

¹Center for Experimental Nanoscale Physics, Department of Physics & Astronomy, University of South Carolina, Columbia, SC 29208, USA. ²Department of Physics & Astronomy, Louisiana State University, Baton Rouge, LA 70803, USA. ³National High Magnetic Field Laboratory, Los Alamos National Laboratory, Los Alamos, NM 87545, USA. ⁴Department of Chemistry, Michigan State University, East Lansing, MI 48824, USA. ✉email: rjin@mailbox.sc.edu

Understanding the interplay between magnetism and nontrivial electronic topology is a new frontier in condensed matter physics^{1–3}. Extensive research has focused on magnetic topological semimetals (MTSMs) with linear electronic energy dispersion in momentum space^{4,5}. Such materials offer unique opportunities to manipulate the electronic band structure and its topology by changing the spin configuration, and are therefore a potential platform for designing new spintronic devices^{6–8}.

Crucial in understanding the formation of nontrivial topological states in semimetals are spin-orbit coupling (SOC), crystal symmetry (\mathcal{PP}), and magnetic ordering, which breaks time-reversal symmetry (\mathcal{TT}). The Dirac state is protected by both \mathcal{PP} and \mathcal{TT} , and can be transformed to a Weyl state through breaking either \mathcal{PP} or \mathcal{TT} . The linear band dispersion in Dirac and Weyl semimetals may contribute to many unusual transport properties, such as large linear magnetoresistance (MR)⁹, ultra-high mobility^{10–13}, chiral anomalies^{14,15}, and the anomalous Hall effect^{16,17}. However, the observation of new quantum phenomena in MTSMs often requires extreme conditions such as high magnetic fields and low temperatures. In addition to quantizing the quasiparticle energy into Landau levels (LLs), external fields may change the magnetic structure of MTSMs, resulting in new states with unusual properties. For example, the quantum Hall effect is only observed in the canted antiferromagnetic state accessed by applying a magnetic field in EuMnBi_2 ¹⁸. On the other hand, higher magnetic fields increase the LL degeneracy, eventually resulting in only the lowest Landau level (LLL) being populated. The combination of the relativistic nature of Weyl/Dirac fermions with these quantum-limit conditions has been linked to emergent quantum phenomena such as interlayer quantum tunneling transport in YbMnBi_2 ¹⁹, a magnetic torque anomaly in the Weyl semimetal NbAs_2 ²⁰, Weyl node annihilation in noncentrosymmetric TaP ²¹, and linear MR after reaching the LLL in Cd_3As_2 ²².

Among known MTSM candidates, Eu-based compounds are unique, as the orientation of the Eu moments is sensitive to the external magnetic field; this scenario is ideal for investigating the effect of magnetic symmetry^{18,23,24}. Of particular interest is the EuM_2As_2 ($M = \text{Cd}, \text{In}, \text{Zn}, \text{etc.}$) material family with nonsymmorphic time-reversal symmetry^{23–25}. A Dirac state is predicted in the antiferromagnetically ordered phase of EuCd_2As_2 ($T_N \approx 8.5 \text{ K}$)²⁴. Experimentally, Weyl nodes have been observed above T_N due to strong ferromagnetic (FM) fluctuations²⁶ or the application of magnetic field²⁴. For EuZn_2As_2 , both T_N and the FM fluctuations regions are doubled compared to EuCd_2As_2 ²³, making it a better platform for studying the interplay between magnetism and topology. In this article, we report the electronic and magnetic properties of EuZn_2As_2 under pulsed magnetic fields of up to 60 T. Giant MR is observed above $\mu_0 H \approx 20 \text{ T}$. By analyzing Shubnikov–de Haas (SdH) and de Haas–van Alphen (dHvA) oscillations, the first LL is reached at $\approx 50 \text{ T}$ for $H \parallel c$, above which the MR becomes linear. Such linear behavior can be explained by the confined Landau wavefunctions within potential minima, resulting in diffusive transport. Our findings help us understand the interplay between magnetism and topological properties and emergent behavior beyond the quantum limit.

Results and discussion

Magnetization, magnetic torque, and proximity detector oscillator (PDO) measurements. EuZn_2As_2 has a trigonal crystal structure ($P\text{-}3m1$, #164) and orders in an A -type spin structure at $T_N = 19 \text{ K}$ ²³. Figure 1a presents the angle dependence of the inverse magnetic susceptibility (χ^{-1}) measured at $\mu_0 H = 0.1 \text{ T}$ (see inset for the definition of the angle ϕ). Note that χ^{-1} decreases linearly with decreasing temperature above $\approx 200 \text{ K}$,

which can be fitted by the Curie–Weiss formula $\chi(T) = \chi_0 + C/(T - \theta)$ (θ is the Curie–Weiss temperature, $C = \frac{\mu_{\text{eff}}^2 N_A}{3k_B}$ is the Curie constant, μ_{eff} is the effective moment, N_A is the Avogadro constant, and k_B is the Boltzmann constant). The obtained θ and μ_{eff} are plotted as a function of angle ϕ in the inset of Fig. 1a. The positive θ suggests FM interaction between Eu ions, with the largest value at $\phi = 45^\circ$. Conversely, μ_{eff} exhibits the smallest value at $\phi = 45^\circ$, likely due to the variation of the SOC. Well below T_N ²³, μ_{eff} obtained at 2 K shows a similar angle dependence. Figure 1b presents the field dependence of the magnetization at $\phi = 45^\circ$, which initially increases linearly with field then becomes saturated (μ_{sat}) at $\mu_0 H_c = 2.4 \text{ T}$. This suggests a continuously increasing Eu moment alignment upon the increase of the magnetic field. As can be seen from the inset of Fig. 1b, both μ_{sat} and $\mu_0 H_c$ show minima at $\phi = 45^\circ$, consistent with that obtained above T_N . These observations confirm that the magnetic easy axis under the magnetic field is at $\phi = 45^\circ$ for EuZn_2As_2 ²³.

While the magnetization appears to saturate above $\mu_0 H_c$, the saturation moment μ_{sat} is lower than μ_{eff} obtained at high temperatures. To clarify this situation, we measure the magnetic torque ($\vec{\tau} = \vec{M} \times \vec{H}$) at higher fields (up to 60 T) and lower temperatures (down to $T = 0.6 \text{ K}$). Figure 1c shows the field dependence of τ at 0.6 K at the indicated angles (the angle ϕ is the same as that defined in the inset of Fig. 1a). Two features may be seen. (1) In the low magnetic field range, there is a sharp rise to $\mu_0 H_c$, the threshold field for the saturated magnetization. (2) The torque decreases monotonically with increasing H when $H > H_c$. Quantitatively, $\tau \propto -H^2$ for $H > H_c$ as shown in Fig. 1d. When all spins are polarized, the torque can be expressed as $|\tau| = \chi_{\text{eff}}(\mu_0 H)^2$, where χ_{eff} is the effective volume susceptibility defined as $\chi_{\text{eff}} = \chi_{ab} - \chi_c$. Similar behavior has been observed in Fe_3Sn_2 , implying that the high-field H^2 behavior corresponds to a constant χ_{eff} ²⁷. Among the measured angles ($3^\circ \leq \phi \leq 48^\circ$), both τ and $\mu_0 H_c$ decrease with increasing ϕ , consistent with the magnetization data (Fig. 1a). Note that the torque does not show any anomaly above $\mu_0 H_c$, suggesting neither a sudden change in the spin orientation nor any other form of metamagnetic transition. To confirm the above observation, we perform proximity detector oscillator (PDO) measurements of EuZn_2As_2 , which is placed on a pancake coil, as shown in the inset of Fig. 1f. This technique is sensitive to the skin or penetration depth in metals or superconductors, and thus can be used to probe the electrical conductivity in such materials²⁸. However, when the resistivity of the material is high, the radiofrequency (RF) field penetrates the whole sample, and the PDO signal (f) becomes more sensitive to the magnetic susceptibility²⁹, i.e., $f \propto dM/dH$ ³⁰. Since EuZn_2As_2 exhibits quite high resistivity²³, the PDO signal is to be dominated by the magnetic properties. To check this, we estimate the skin depth δ via the equation $\delta = \sqrt{\frac{2\rho}{\omega\mu}}$, where ρ is the resistivity, ω the angular frequency and μ the permeability³¹. Using $\rho(2 \text{ K}) = 30 \text{ m}\Omega \text{ cm}$ and $\omega/2\pi = 25 \text{ MHz}$ (the PDO frequency), we obtain $\delta \approx 2 \text{ mm}$. Since the typical sample dimensions are less than 1 mm, the RF field penetrates the whole sample. Further support for this assertion, i.e., the PDO response is chiefly determined by dM/dH , comes from the overall form of the PDO data, which can be seen to closely resemble the differential of the magnetization, and the phase of the quantum oscillations in the PDO signal compared to those in the MR (see below).

Figure 1e shows the magnetic field dependence of the PDO frequency f , plotted as $f - f_0$, with f_0 being the frequency at $H = 0$ at $T = 0.6 \text{ K}$ and indicated angles (the angle ϕ_{ac} is defined in the inset of Fig. 1f). Features occur at similar fields to those observed in the magnetic torque, i.e., there is a sharp rise at H_c . However,

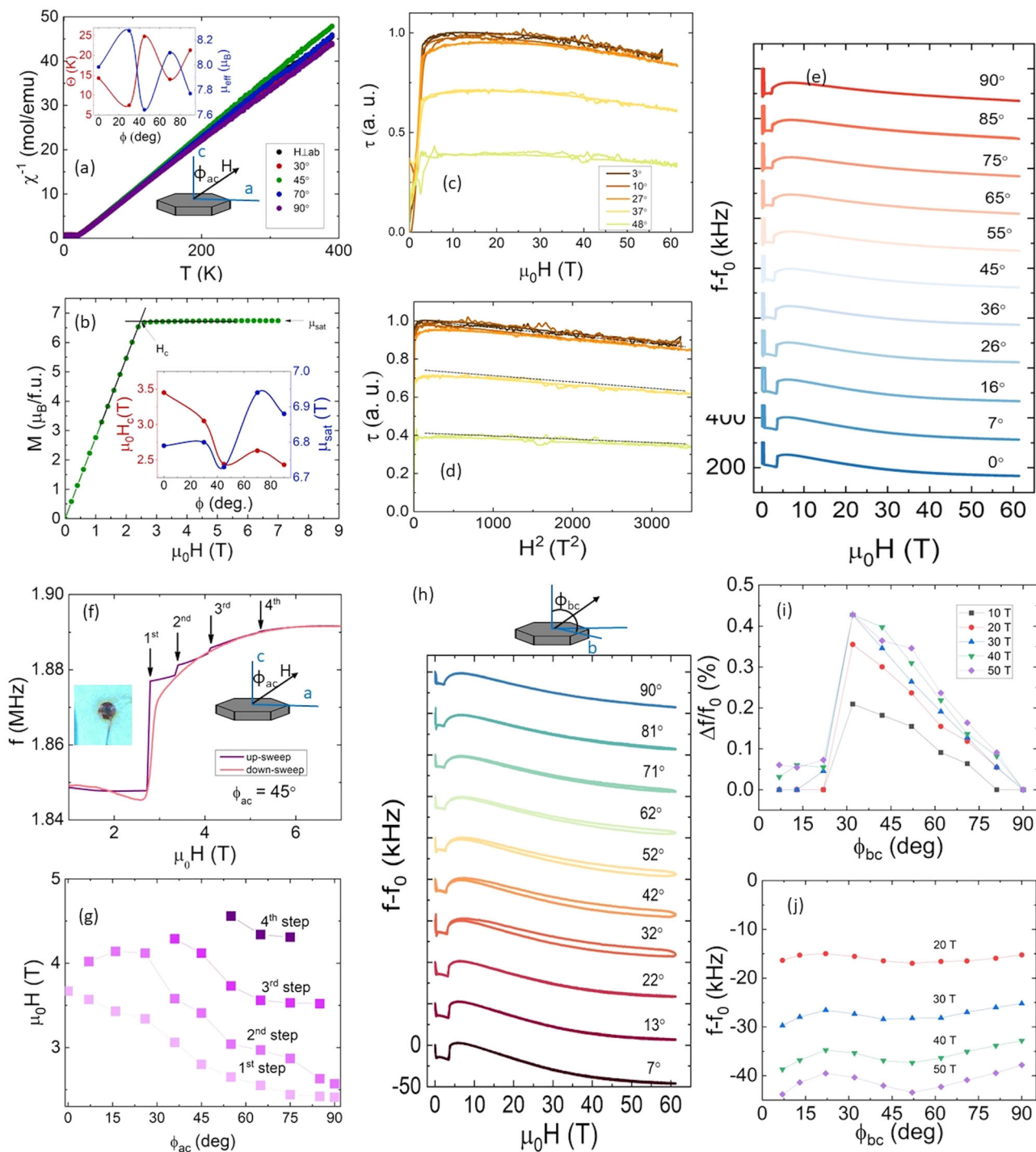


Fig. 1 Magnetic properties. **a** Inverse magnetic susceptibility versus temperature at indicated angles. Inset: The Curie-Weiss temperature and effective magnetic moment versus angle. **b** Magnetization as a function of magnetic field at $\phi = 45^\circ$. Inset: Saturation moment and magnetic field transition versus angle. **c** Magnetic field dependence of the torque taken at various angles. **d** Torque versus H^2 with a dashed line for eye guidelines. **e** Proximity detector oscillation (PDO) frequency as a function of magnetic field taken at various angles. **f** Low magnetic field region of PDO frequency at $\phi = 45^\circ$ pointing the step-like behavior. Inset: PDO pancake coil. **g** Magnetic field value at each step versus magnetic field taken at various angles. **h** PDO signal as a function of magnetic field taken at various angles. **i** Normalized difference between raising and falling field curves as a function of angle taken at fixed magnetic fields. **j** PDO frequency versus angle at fixed magnetic fields.

on closer inspection, one can find new features unseen previously. Figure 1f presents $f(H)$ in rising (upsweep) and falling (down-sweep) magnetic fields at $\phi_{ac} = 45^\circ$. As the field rises, $f(H)$ shows staircase-like steps as indicated by arrows. The corresponding magnetic fields decrease with increasing angle ϕ_{ac} , as shown in Fig. 1g. This and the smooth $f(H)$ measured as the field decreases

suggest that the step-like behavior results from the growth of FM domains or clusters; populations of different clusters become ferromagnetically ordered at slightly different fields that depend sensitively on the local microscopic arrangement of the moments³². This results in several steps followed by the fully polarized state of the whole sample.

The staircase-like steps appear in the pulsed-field experiments and are not observed in steady-field measurements or torque. Moreover, their presence depends on the sweep rate of the magnetic field. We did not observe staircase-like steps at slower sweep rates (10 T magnet pulses), but they are visible at higher sweep rates (60 T pulses). Analogous sweep-rate-dependent transient phenomena in magnetization, including plateaus, have been reported in other magnetic materials^{32,33} and attributed to local microscopic variations in the arrangements of the magnetic moments. The fact that the PDO is sensitive to dM/dH , the differential of the magnetization, means that the resulting tiny, sharp features will tend to show up much more strongly than they do in (undifferentiated) torque or magnetization data, as is the case here.

Returning to the angle dependence of the critical fields corresponding to the steps [Fig. 1g], we note that these fields decrease with increasing ϕ_{ac} , consistent with an *A*-type spin structure at zero field. In other words, the FM domain alignment requires smaller fields for $H \parallel ab$ ($\phi_{ac} = 90^\circ$) than for $H \parallel c$ ($\phi_{ac} = 0^\circ$).

Given its trigonal crystal symmetry and the magnetic moment pointing to the *a*-axis in EuZn_2As_2 ²³, we perform PDO measurements in another configuration: varying the field angle ϕ_{bc} in the *bc* plane (30° away from the *a*-axis) as illustrated in the inset of Fig. 1h. Figure 1h shows the PDO frequency as a function of the magnetic field at the indicated angles (ϕ_{bc}). While overall features are similar to those in Fig. 1e, the staircase-like behavior is absent in both the up- and down-sweeps. Instead, a hysteresis loop is observed between upsweep and downsweep curves. Figure 1i plots the difference in the frequency between up- and down-sweeps at fixed fields as a function of the angle ϕ_{bc} . Note the magnitude of hysteresis has a similar angle dependence in all fields, peaking around $\phi_{bc} \approx 30^\circ$. This suggests that the most difficult FM domain alignment is along $\phi_{bc} \approx 30^\circ$, i.e., this represents the magnetic hard axis. This is further proven by plotting the angle dependence of $f - f_0$ at fixed fields, as shown in Fig. 1j. The nonmonotonic angle dependence of $f - f_0$ implies that the field-induced spin rearrangement depends on the direction of the applied field. The maximum $|f - f_0|$ around 50° corresponds to large dM/dH .

While $f(H)$ seems at first sight smooth, without any features above H_c , quantum oscillations can be seen above $\mu_0 H = 20$ T after background (bg) subtraction. Figure 2a shows the dHvA oscillation signal $\Delta f = (f - f_0) - (f - f_0)_{bg}$ as a function of the inverse magnetic field at the indicated angles (ϕ_{ac}). Fast Fourier transformation (FFT) reveals a single frequency $F(\phi_{ac} = 0) \approx 47$ Tesla, as illustrated by the red dashed curve in Fig. 2b, which represents the principal oscillatory part of the Lifshitz–Kosevich (LK) formula $\Delta f \propto A \sin(2\pi F/H + \beta)$. Since $\Delta f \propto \Delta M/\Delta H$ in our case, the minimum is assigned to integer LL (*N*) quantum number and the maximum to $N + 1/2$. The doubling of each peak indicates Zeeman spin-splitting, which splits the LLs into spin-up (N^+) and spin-down (N^-) halves. A Landau fan diagram is constructed in Fig. 2c for $\phi_{ac} = 0^\circ$. The phase factor difference $\beta(\text{spin-up}) - \beta(\text{spin-down}) = 0.31 = gm^*/2m_0$, where *g* is the Lande factor and m^* and m_0 are the effective and free electron masses, respectively.

Magnetotransport measurements. To confirm the quantum oscillations observed in PDO measurements, we have further measured the magnetic field dependence of the $MR = \frac{\rho(H) - \rho(H=0)}{\rho(H=0)} \times 100\%$ up to 60 T at the indicated angles. After careful background (R_{bg}) subtraction using a polynomial function, resistance oscillations may be observed above ≈ 15 T.

Figure 2d shows the Shubnikov-de Haas (SdH) oscillations at $T = 0.6$ K and indicated angles (ϕ_{ac}). For simplicity, we plot the oscillatory $\Delta R/R_{bg}$ as a function of $1/\mu_0 H$ at $\phi_{ac} = 5^\circ$ and $T = 0.6$ K in Fig. 2e. FFT reveals a single frequency $F \approx 46$ Tesla, very close to that obtained from PDO data (Fig. 2b). The red dashed curve represents the principal oscillatory part of the LK formula $\Delta R \propto A \cos(2\pi F/H + \beta)$ where $A(H, T)$ is the oscillation amplitude and β is the phase factor. Similar to that seen in the dHvA oscillations, the Zeeman splitting results in the doubling of peaks. A Landau fan diagram can be constructed by assigning the maxima to integer *N* and the minimum to $N + 1/2$. Figure 2f shows the Landau fan diagram using data displayed in Fig. 2e for $\phi_{ac} = 5^\circ$ at $T = 0.6$ K with integer *N* from spin-up levels (N^+ : black dots) and spin-down levels (N^- : blue dots) and $N + 1/2$ and *N* levels from the LK formula simulation (red dots). We fit the data from the plot using the Lifshitz–Ongsager quantization criterion $N = F/H + \beta$ ³⁴, which gives $F = 39$ T and $\beta = 0.37$ for $\phi_{ac} = 5^\circ$ at $T = 0.6$ K. Both $N^+(H)$ and $N^-(H)$ can be fitted by the Lifshitz–Ongsager relationship with the phase factor difference $\beta(\text{spin-up}) - \beta(\text{spin-down}) = 0.39 = gm^*/2m_0$.

Figure 2g shows the angle dependence of the averaged frequency obtained from SdH and dHvA oscillations. Compared to EuCd_2As_2 , the calculated frequency *F* for EuZn_2As_2 is larger. According to the Ongsager relation $F = \left(\frac{\phi_0}{2\pi^2}\right)S$, where ϕ_0 is the flux quantum and *S* is the cross-sectional area of the Fermi surface normal to the magnetic field direction, a large *F* corresponds to a large *S*. For $\phi = -1^\circ$, the cross-section area $S = 0.36 \text{ nm}^{-2}$. In a similar field configuration, $S = 0.24 \text{ nm}^{-2}$ for EuCd_2As_2 ²⁴.

The nonmonotonic angle dependence of *F* reflects the three-dimensional shape of the Fermi surface. Our observations suggest that the Fermi surface (and therefore band structure) of EuZn_2As_2 is similar to that of EuCd_2As_2 ³⁵. However, the Eu bands are located at higher energy³⁶, resulting in a larger bulk band gap in EuZn_2As_2 . According to Hall effect measurements, the transport in EuZn_2As_2 is dominated by holes²³. Therefore, the observed SdH oscillations probably correspond to the hole band with an irregular ring shape also predicted for EuCd_2Sb_2 ³⁷. The relative sizes of the Fermi-surface cross-sections derived above imply that EuZn_2As_2 has a larger population of holes than does EuCd_2As_2 . In view of the band structure of EuZn_2As_2 ³⁵, our results, therefore, suggest that the Fermi energy for our sample is lower than that calculated one.

For such a hole Fermi surface, we can write $\beta = \Phi_B/2\pi - 1/8$ ³⁴, where Φ_B is the Berry phase. The angle dependence of an average Φ_B is plotted in Fig. 2g, which shows non-zero Φ_B in all angles. This implies nontrivial electronic topology. An anisotropic Berry phase was also observed in other topological materials, such as ZrSiS . It was suggested that the strong SOC can induce a finite gap, which will not change the topology of the electronic structure but may result in a modification of the Berry phase^{36,38}.

The temperature dependence of the SdH oscillation amplitude was measured up to 40 K as shown in Fig. 2h. By fitting data to the LK formula, amplitude $A \propto \chi/\sinh\chi$, where $\chi = 2\pi^2 k_B T m^*/ehH$, and $m^* = (\hbar^2/2\pi)dS/dE$, the effective mass $m^* = 0.07m_0$ is obtained, which is slightly smaller than the one obtained for EuCd_2As_2 . Considering the phase factor difference $\beta(\text{spin-up}) - \beta(\text{spin-down}) = gm^*/2m_0$, we can estimate $g \approx 11$, which is much larger than that expected for free electrons ($g = 2$). Enhanced *g* factors have been previously observed in other Dirac and Weyl semimetals, such as ZrSiS ³⁹, Cd_3As_2 ⁴⁰, and ZrTe_5 ⁴¹, and attributed to strong SOC^{41,42}.

Figure 3 shows the magnetic field dependence of the $MR = \frac{\rho(H) - \rho(H=0)}{\rho(H=0)} \times 100\%$ at $T = 0.6$ K up to 60 T at the indicated angles.

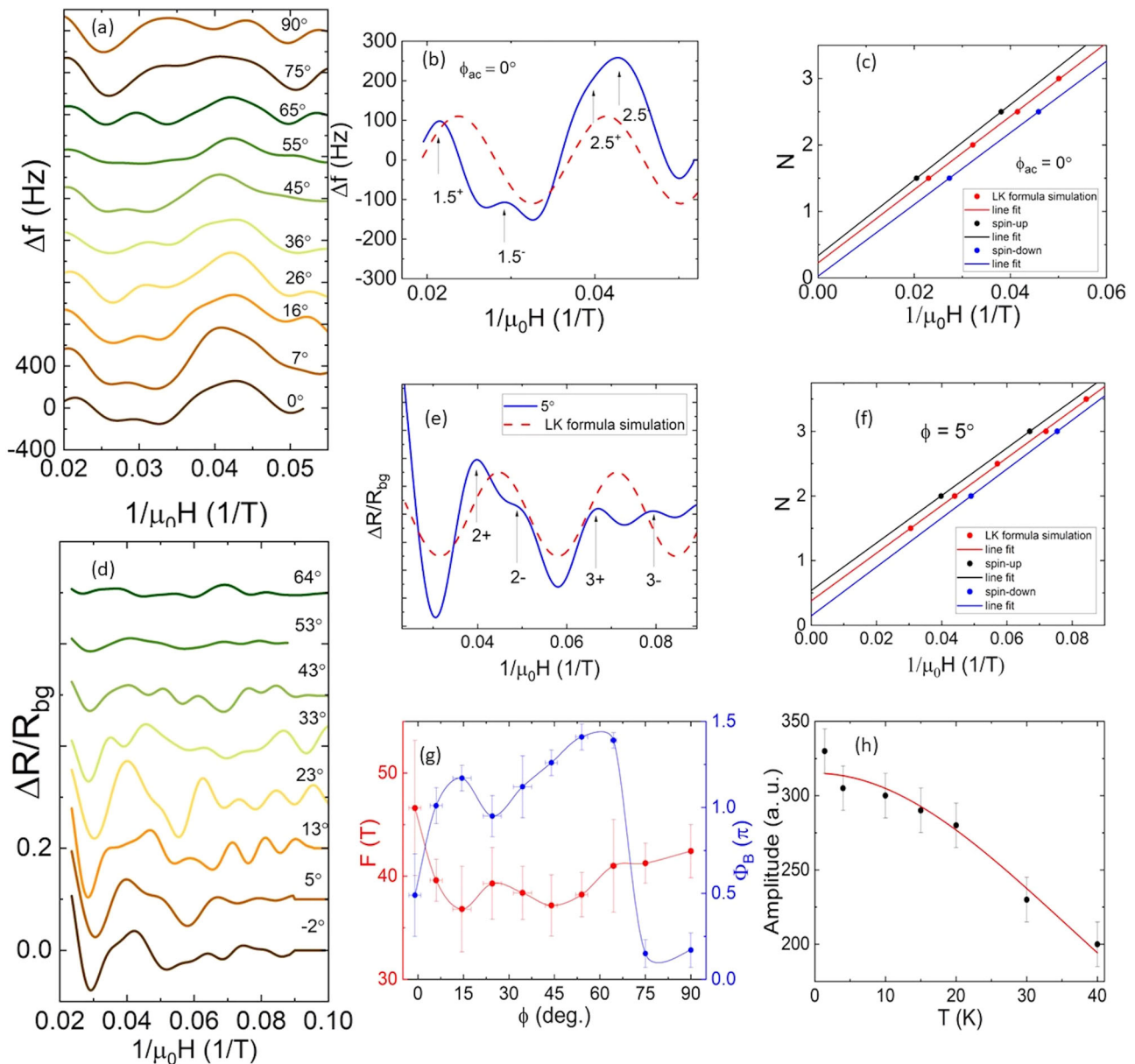


Fig. 2 Quantum oscillations. **a** de Haas-van Alphen (dHvA) quantum oscillation as a function of the magnetic field at various angles. **b** dHvA quantum oscillation as a function of the inverse magnetic field at $\phi = 0^\circ$ (blue line) and the simulation of dHvA oscillation described by Lifshitz-Kosevich (LK) formula (red dashed line). **c** Landau fan diagram for oscillation at $\phi = 0^\circ$. **d** Shubnikov-de Haas (SdH) quantum oscillation as a function of the magnetic field at various angles. **e** SdH quantum oscillation as a function of the inverse magnetic field at $\phi = 5^\circ$ (blue line) and the simulation of SdH oscillation described by LK formula (red dashed line). **f** Landau fan diagram for oscillation at $\phi = 5^\circ$. **g** Left: frequency versus angle, right: Berry phase as a function of angle. Error bars for both quantities are determined through the fit of the Landau fan diagram to the Lifshitz-Onsager quantization criterion described in the section of Magnetotransport Measurements. **h** Temperature dependence of the amplitude in the SdH oscillations. The red line represents the fit of data to the Lifshitz-Kosevich formula described in the section of Magnetotransport Measurements. The error bar is the standard deviation due to the subtraction of the background.

In addition to the previously reported feature observed at low fields²³, new phenomena in the MR are observed at high fields. First, the MR at each angle remains constant between $\mu_0 H_c$ and approximately 35 Tesla. Above 35 T, the MR increases gradually with increasing field, reaching $\approx 1000\%$ for $H \parallel c$. While the magnitude strongly depends on the applied field direction, with a minimum around $\phi \approx 50^\circ$ (see the inset of Fig. 3), the MR shows no sign of saturation up to 60 Tesla. In fact, above $\mu_0 H \approx 50$ T, the MR exhibits a linear field dependence. The minimum MR angle ($\phi \approx 45^\circ$) is in accord with the torque, magnetization, and low-field MR, confirming the magnetic easy axis is close to 45° . However, considering the monotonic field dependence of the

torque above $\mu_0 H_c$ (Fig. 1c), the speedy rise of the MR above ≈ 35 Tesla cannot not be related to any rearrangement of the magnetic moments.

At all orientations, from the Landau fan diagram shown in Fig. 2c and the SdH and dHvA frequencies, the quasiparticles are in the LLL by $\mu_0 H \approx 50$ T. For all applied field directions, the MR increases with a field without a sign of saturation up to 60 T. Notably, the MR depends linearly on H for $\phi = -2^\circ$. According to Abrikosov theory⁴³, linear MR occurs in the quantum limit due to the linear energy-momentum dispersion relationship. Similar quantum-limit (QL) behavior has been observed in Cd_3As_2 above 43 T²². According to recent calculations⁴⁴, linear MR occurs in a

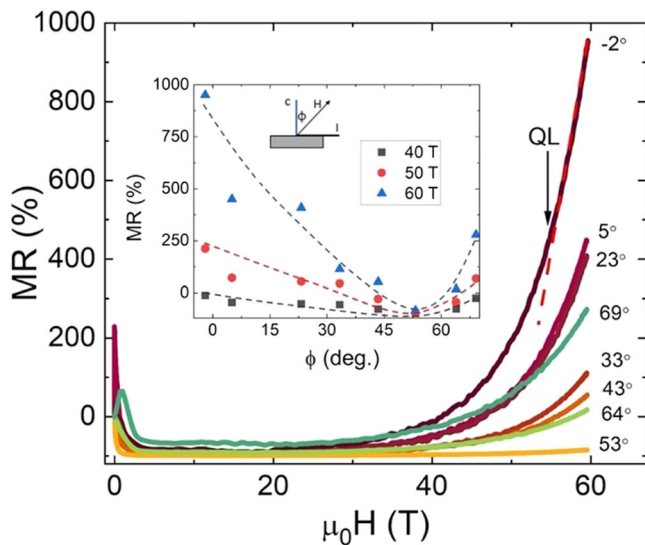


Fig. 3 Linear quantum MR. Magnetoresistivity (MR) as a function of the magnetic field at indicated angles, where QL denotes quantum limit. Inset: MR at fixed magnetic field versus angle at $T = 0.6$ K, where the angle is between the crystallographic c direction and the applied magnetic field H . I denotes the current.

fully compensated semimetal when the scattering potential is smooth within the magnetic length scale $l_m = \sqrt{(2N+1)\hbar/eH}$; effectively, the Landau wavefunctions are confined within potential minima, resulting in diffusive transport where the resistivity is proportional to $l_m^{-2} \propto H^{-1}$. When EuZn_2As_2 reaches the first LL ($N=1$) just below 50 T for $H \parallel c$, $l_m \approx 6$ nm, suggesting a length scale of this approximate size for the disorder potential for motion within the ab planes. However, when H is rotated towards the ab plane, the Landau orbits will tilt, forcing the quasiparticles to move in and out of the ab planes, thereby encountering a different disorder landscape. For example, for $H \parallel ab$, the scattering potential cannot be smooth within l_m due to the layered structure of EuZn_2As_2 , which possesses an interlayer distance ≈ 0.7175 nm²³. It is the variation of the typical length scale of the potential landscape encountered by the tilted cyclotron orbits that results in the observed angle dependence of the MR.

Conclusion

In summary, we have experimentally investigated the electronic and magnetic properties of EuZn_2As_2 , an MTSM candidate, in pulsed magnetic fields of up to 60 T. Giant positive MR is observed above $\mu_0 H \approx 20$ T; however, magnetic torque and PDO measurements show no corresponding anomaly. By analyzing the SdH and dHvA oscillations between 15 and 50 T, we obtain the oscillation frequency $F = 46$ Tesla for $H \parallel c$, whilst observing clear Zeeman splitting of the oscillations attributable to a substantially enhanced g -factor. The oscillation frequency extracted from both SdH and dHvA oscillations is nearly independent of angle within the error bars with the angle between the c axis and the ab plane, demonstrating the almost isotropic hole band shape of EuZn_2As_2 . While the Berry phase extracted from the Landau phase diagram varies with the angle as well, a consistently non-zero Φ_b indicates the nontrivial topology of this hole band.

From both the quantum-oscillation frequencies and Landau fan diagrams, it is clear that only the first LL is occupied by 50 T. Above this field, the MR varies linearly with H , without any sign of saturation. This is attributable to the quantum-limit mechanism originally due to Abrikosov and further developed in ref. 44,

where compressed Landau wavefunctions are confined by smooth potential fluctuations, resulting in diffusive transport. The field-angle dependence of the large MR demonstrates the varying disorder potential length scales that exist in layered EuZn_2As_2 . Our findings help us understand the interplay between magnetism, topological properties, disorder, and emergent behavior in the quantum limit.

Methods

Single crystals of EuZn_2As_2 were synthesized by the flux method as described in ref. 23. Elemental Eu (99.9%, Alfa Aesar), Zn (99.8%, Alfa Aesar), As (99.999%, Alfa Aesar), and Sn (99.9%, Alfa Aesar) were mixed with a molar ratio $\text{Eu}:\text{Zn}:\text{As}:\text{Sn} = 1:2:2:20$, and then sealed in an evacuated quartz tube. The sample was heated up to 600 °C at a rate of 60 °C h⁻¹ and kept at this temperature for 5 h, followed by staying at 1000 °C for 10 h. The sample was then slowly cooled (−3 °C h⁻¹) down to 600 °C with a further centrifuge to remove Sn flux. The low-field magnetic properties were measured in a Quantum Design Magnetic Properties Measurement System (7 T), while the high-field data were taken at the pulsed-field facility of the National High Magnetic Field Laboratory (NHMFL, Los Alamos). Standard four-probe techniques were used to measure the MR. Four thin Pt wires were placed on a sample using silver epoxy, and each Pt wire was attached to 50-gauge copper wire. The copper wires were twisted in pairs (current pair and voltage pair) to reduce electrical noise. Samples were placed on a cryogenic goniometer (fabricated using additive manufacturing techniques⁴⁵) for measurements at different angles in the pulsed magnetic fields. An AC current of 0.23 mA was applied at 50 kHz frequency; care was taken to ensure that this did not cause heating in the sample. The torque measurements were carried out in magnetic fields of up to 60 T by mounting a 50- μm -long crystal on a piezoresistive cantilever⁴⁶. For performing PDO measurements, a sample was placed on the top of an 8-turn coil made of 46-gauge copper wire. The coil is connected to the PDO circuit which has a resonant frequency in the range of 22–30 MHz determined by the sample's conductivity and, to a lesser extent, its magnetic susceptibility³⁰.

Data availability

The source data and related supporting information are available upon reasonable request from the corresponding author.

Received: 19 April 2023; Accepted: 7 September 2023;

Published online: 16 September 2023

References

- Keimer, B. & Moore, J. E. The physics of quantum materials. *Nat. Phys.* **13**, 1045–1055 (2017).
- Hasan, M. Z., Xu, S.-Y. & Bian, G. Topological insulators, topological superconductors and Weyl fermion semimetals: discoveries, perspectives and outlooks. *Phys. Scr.* **T164**, 014001 (2015).
- Liao, Z., Jiang, P., Zhong, Z. & Li, R.-W. Materials with strong spin-textured bands. *npj Quantum Mater.* **5**, 1–10 (2020).
- Vafeek, O. & Vishwanath, A. Dirac fermions in solids: from high- T_c cuprates and graphene to topological insulators and Weyl semimetals. *Annu. Rev. Condens. Matter Phys.* **5**, 83–112 (2014).
- Armitage, N. P., Mele, E. J. & Vishwanath, A. Weyl and Dirac semimetals in three-dimensional solids. *Rev. Mod. Phys.* **90**, 015001 (2018).
- Šmejkal, L., Mokrousov, Y., Yan, B. & MacDonald, A. H. Topological antiferromagnetic spintronics. *Nat. Phys.* **14**, 242–251 (2018).
- Hasan, M. Z. et al. Weyl, Dirac and high-fold chiral fermions in topological quantum matter. *Nat. Rev. Mater.* **6**, 784–803 (2021).
- Bernevig, B. A., Felser, C. & Beidenkopf, H. Progress and prospects in magnetic topological materials. *Nature* **603**, 41–51 (2022).

9. Feng, J. et al. Large linear magnetoresistance in Dirac semimetal Cd_3As_2 with Fermi surfaces close to the Dirac points. *Phys. Rev. B* **92**, 081306 (2015).
10. Liang, T. et al. Ultrahigh mobility and giant magnetoresistance in the Dirac semimetal Cd_3As_2 . *Nat. Mater.* **14**, 280–284 (2015).
11. Xiong, J. et al. Anomalous conductivity tensor in the Dirac semimetal Na_3Bi . *EPL* **114**, 27002 (2016).
12. Huang, S., Kim, J., Shelton, W. A., Plummer, E. W. & Jin, R. Nontrivial Berry phase in magnetic BaMnSb_2 semimetal. *Proc. Natl Acad. Sci. USA* **114**, 6256–6261 (2017).
13. Us Saleheen, A. I. et al. Evidence for topological semimetallicity in a chain-compound TaSe_3 . *npj Quantum Mater.* **5**, 1–8 (2020).
14. Burkov, A. A. Chiral anomaly and diffusive magnetotransport in Weyl metals. *Phys. Rev. Lett.* **113**, 247203 (2014).
15. Hirschberger, M. et al. The chiral anomaly and thermopower of Weyl fermions in the half-Heusler GdPtBi . *Nat. Mater.* **15**, 1161–1165 (2016).
16. Manna, K. et al. From colossal to zero: controlling the anomalous Hall effect in magnetic heusler compounds via Berry curvature design. *Phys. Rev. X* **8**, 041045 (2018).
17. Wang, Q. et al. Large intrinsic anomalous Hall effect in half-metallic ferromagnet $\text{Co}_3\text{Sn}_2\text{S}_2$ with magnetic Weyl fermions. *Nat. Commun.* **9**, 3681 (2018).
18. Masuda, H. et al. Quantum Hall effect in a bulk antiferromagnet EuMnBi_2 with magnetically confined two-dimensional Dirac fermions. *Sci. Adv.* **2**, e1501117 (2016).
19. Liu, J. Y. et al. Unusual interlayer quantum transport behavior caused by the zeroth Landau level in YbMnBi_2 . *Nat. Commun.* **8**, 646 (2017).
20. Moll, P. J. W. et al. Magnetic torque anomaly in the quantum limit of Weyl semimetals. *Nat. Commun.* **7**, 12492 (2016).
21. Zhang, C.-L. et al. Magnetic-tunnelling-induced Weyl node annihilation in TaP . *Nat. Phys.* **13**, 979–986 (2017).
22. Zhao, Y. et al. Anisotropic fermi surface and quantum limit transport in high mobility three-dimensional dirac semimetal Cd_3As_2 . *Phys. Rev. X* **5**, 031037 (2015).
23. Blawat, J. et al. Unusual electrical and magnetic properties in layered EuZn_2As_2 . *Adv. Quantum Technol.* **5**, 2200012 (2022).
24. Soh, J.-R. et al. Ideal Weyl semimetal induced by magnetic exchange. *Phys. Rev. B* **100**, 201102 (2019).
25. Hua, G. et al. Dirac semimetal in type-IV magnetic space groups. *Phys. Rev. B* **98**, 201116 (2018).
26. Ma, J.-Z. et al. Spin fluctuation induced Weyl semimetal state in the paramagnetic phase of EuCd_2As_2 . *Sci. Adv.* **5**, eaaw4718 (2019).
27. Ye, L. et al. de Haas-van Alphen effect of correlated Dirac states in kagome metal Fe_3Sn_2 . *Nat. Commun.* **10**, 4870 (2019).
28. Altarawneh, M. M., Mielke, C. H. & Brooks, J. S. Proximity detector circuits: An alternative to tunnel diode oscillators for contactless measurements in pulsed magnetic field environments. *Rev. Sci. Instrum.* **80**, 066104 (2009).
29. Coffey, T. et al. Measuring radio frequency properties of materials in pulsed magnetic fields with a tunnel diode oscillator. *Rev. Sci. Instrum.* **71**, 4600–4606 (2000).
30. Ghannadzadeh, S. et al. Measurement of magnetic susceptibility in pulsed magnetic fields using a proximity detector oscillator. *Rev. Sci. Instrum.* **82**, 113902 (2011).
31. Staelin, D. H. *Electromagnetics and Applications* (MIT, 2011).
32. Narumi, Y. et al. Observation of a transient magnetization plateau in a quantum antiferromagnet on the Kagome lattice. *Europhys. Lett.* **65**, 705–711 (2004).
33. Singleton, J. et al. Magnetic properties of $\text{Sr}_3\text{NiIrO}_6$ and $\text{Sr}_3\text{CoIrO}_6$: magnetic hysteresis with coercive fields of up to 55 T. *Phys. Rev. B* **94**, 224408 (2016).
34. Shoenberg, D. *Magnetic Oscillations in Metals* (Cambridge University Press, 2009).
35. Wang, Z.-C. et al. Anisotropy of the magnetic and transport properties of EuZn_2As_2 . *Phys. Rev. B* **105**, 165122 (2022).
36. Ali, M. N. et al. Butterfly magnetoresistance, quasi-2D Dirac Fermi surface and topological phase transition in ZrSiS . *Sci. Adv.* **2**, e1601742 (2016).
37. Soh, J.-R. et al. Magnetic and electronic structure of the layered rare-earth pnictide EuCd_2Sb_2 . *Phys. Rev. B* **98**, 064419 (2018).
38. Yang, Y. et al. Anisotropic Berry phase in the Dirac nodal-line semimetal ZrSiS : the effect of spin-orbit coupling. *Phys. Rev. B* **103**, 125160 (2021).
39. Hu, J. et al. Nearly massless Dirac fermions and strong Zeeman splitting in the nodal-line semimetal ZrSiS probed by de Haas-van Alphen quantum oscillations. *Phys. Rev. B* **96**, 045127 (2017).
40. Cao, J. et al. Landau level splitting in Cd_3As_2 under high magnetic fields. *Nat. Commun.* **6**, 7779 (2015).
41. Liu, Y. et al. Zeeman splitting and dynamical mass generation in Dirac semimetal ZrTe_5 . *Nat. Commun.* **7**, 12516 (2016).
42. Fuseya, Y. et al. Origin of the large anisotropic g factor of holes in Bismuth. *Phys. Rev. Lett.* **115**, 216401 (2015).
43. Abrikosov, A. A. Quantum magnetoresistance. *Phys. Rev. B* **58**, 2788–2794 (1998).
44. Kazantsev, A., Berdyugin, A., Geim, A. & Principi, A. On the origin of Abrikosov’s quantum linear magnetoresistance. Preprint at <http://arxiv.org/abs/2208.06273> (2022).
45. Willis, X., Ding, X., Singleton, J. & Balakirev, F. F. Cryogenic goniometer for measurements in pulsed magnetic fields fabricated via additive manufacturing technique. *Rev. Sci. Instrum.* **91**, 036102 (2020).
46. Ohmichi, E. & Osada, T. Torque magnetometry in pulsed magnetic fields with use of a commercial microcantilever. *Rev. Sci. Instrum.* **73**, 3022–3026 (2002).

Acknowledgements

Work at the University of South Carolina and Louisiana State University was supported by NSF through Grant DMR-1504226. A portion of this work was performed at the National High Magnetic Field Laboratory (NHMFL), which is supported by National Science Foundation Cooperative Agreement Nos. DMR-1644779 and the Department of Energy (DOE). J.S. acknowledges support from the DOE BES program “Science at 100T,” which permitted the design and construction of specialized equipment used in the high-field studies.

Author contributions

R.J. and J.B. proposed and designed the research. J.B. and W.X. synthesized the single crystals. J.B. carried out the low magnetic field measurements and data analysis. J.S., J.B., and S.S. carried out the high magnetic field measurements and data analysis. J.B., R.J., and J.S. wrote the paper with input from all co-authors. R.J. oversaw the project.

Competing interests

The authors declare no competing interests.

Additional information

Supplementary information The online version contains supplementary material available at <https://doi.org/10.1038/s42005-023-01378-8>.

Correspondence and requests for materials should be addressed to Rongying Jin.

Peer review information *Communications Physics* thanks the anonymous reviewers for their contribution to the peer review of this work. A peer review report is available.

Reprints and permission information is available at <http://www.nature.com/reprints>

Publisher’s note Springer Nature remains neutral with regard to jurisdictional claims in published maps and institutional affiliations.



Open Access This article is licensed under a Creative Commons Attribution 4.0 International License, which permits use, sharing, adaptation, distribution and reproduction in any medium or format, as long as you give appropriate credit to the original author(s) and the source, provide a link to the Creative Commons licence, and indicate if changes were made. The images or other third party material in this article are included in the article’s Creative Commons licence, unless indicated otherwise in a credit line to the material. If material is not included in the article’s Creative Commons licence and your intended use is not permitted by statutory regulation or exceeds the permitted use, you will need to obtain permission directly from the copyright holder. To view a copy of this licence, visit <http://creativecommons.org/licenses/by/4.0/>.

© The Author(s) 2023